Hindawi
Journal of Sensors
Volume 2021, Article ID 9986523, 11 pages
https://doi.org/10.1155/2021/9986523

Research Article

Influence of Swell Wave on Wind Speed Retrieval Using ENVISAT ASAR Wave Mode Imagery

Duo Wang,[1,2,3] Xiaochen Wang ,[1,2] and Weili Jiao[1,2]

[1]*Aerospace Information Research Institute, Chinese Academy of Science, Beijing 100190, China*
[2]*University of Chinese Academy of Sciences, Beijing 100049, China*
[3]*The State Geospatial Information Center, Beijing 100835, China*

Correspondence should be addressed to Xiaochen Wang; wangxc@radi.ac.cn

Received 29 March 2021; Revised 19 June 2021; Accepted 23 July 2021; Published 15 October 2021

Academic Editor: Abdellah Touhafi

The main work of this paper is to explore the influence of swell wave on retrieval of wind speed using ENVISAT ASAR wave mode imagery. The normalized radar cross section (NRCS) scene under different sea states is simulated to investigate the relationship between NRCS variation with swell height, together with swell direction. Moreover, the key parameter of imagery variance (Cvar) is selected to describe the swell wave on SAR imagery. In addition, the imagery parameters of skewness and kurtosis are together analyzed as a function of collocated significant swell wave height and wind speed. Based on the analyzed results, a new method for wind speed retrieval is proposed using ENVISAT ASAR, namely, F(n). Besides the CMOD parameters of NRCS, incidence angle, and relative wind direction, the imagery parameters of Cvar, skewness, and kurtosis are used to compensate for the influence of swell wave on wind speed retrieval in F(n). Finally, the collocated European Centre for Medium-Range Weather Forecast (ECMWF) wind speed dataset and ENVISAT ASAR wave mode imagery are used to verify the retrieval precision and compare with CMOD functions. It is concluded that the F(n) model performs much better than other CMOD functions, with a correlation of 0.89, a bias of 0.08, a RMSE of 1.2 m/s, and an SI of 0.1.

1. Introduction

Over the past decades, multiple space-borne SAR platforms have been launched and operated for sea surface monitoring, especially for retrieval of wind vector field. For a SAR platform which operates in VV, VH, HV, and HH polarization, the semiempirical geophysical model functions (GMFs) are adapted to retrieve wind vector, such as SEASAT, ERS-1/2, ENVISAT ASAR, RADARSAT-1/2, SENTINEL-1 A/B, and GF-3. The principle of GMFs is to build a complicated relationship between the normalized radar cross section (NRCS) of copolarization SAR and wind vectors at 10 m above the sea surface [1–3]. Among all the widely used GMFs, the C-band CMOD series function is mainly used to invert the wind speed from sea surface backscatter signals [4]. It is proven that the CMOD functions work well for wind retrieval from SAR at C-band and well validated at wind speed ranges from 0 to 20 m/s. However, unsatisfying retrieval results of CMODs appear in extreme sea states with wind speeds above 20 m/s [5, 6]. To solve this, the response of high wind speed to cross-polarization signal is also used to resolve the saturation of sea surface NRCS in a high wind speed situation [7, 8].

Based on the CMOD functions, many researchers developed an adaptive method for operated SAR data. The CMOD2 model is established by using the ERS-1 scatterometer airborne test observation [9]. After the launch of ERS-1, it was found that the CMOD2 model is not applicable to the observations of the ERS-1 on-board scatterometer, and the CMOD4 model was developed by using the observations of the ERS-1 on-board scatterometer [10]. Then, the CMOD2-IFR2 model was developed by using ERS-1 scatterometer observations [11]. Although the sea surface wind field based on the CMOD4 model inversion meets the accuracy requirements (RMS error of wind speed is less than 2 m/s, and RMS error of wind direction is less than 20°), it is underestimated in general, especially in the case of high wind speed. In order to correct the shortcomings of the

COMD4 model, the CMOD5 model was developed based on ERS-2 scatterometer observations, which improves the applicability to high wind speed [12]. In order to get the neutral wind rather than the real wind, the coefficient of the CMOD5 model is refitted and the CMOD5.N model is obtained [13]. Moreover, a modified CMOD5.H model by using ASCAT scatterometer high wind speed observations is also proposed [14]. Then, the CMOD5.N model was further modified by using ASCAT scatterometer observations to develop the CMOD6 model, and it has been proven that the model is applicable to all C-band satellite scatterometer observations such as ERS and ASCAT [15]. Finally, the CMOD7 model was developed based on cross-calibrated ERS and ASCAT scatterometer data, and its overall performance is better than that of the CMOD5.N model [16].

Considering that CMOD functions were mainly derived from space-borne scatterometer measurements, more CMOD functions directly derived from SAR measurements are proposed for wind speed retrieval. Due to the global massive collection of ENVISAT ASAR data, an initial SAR GMF, denoted CSARMOD, was derived from collocated ENVISAT ASAR-measured NRCS and wind speed and direction data acquired by ASCAT [17]. However, CSARMOD is not applied to any SAR wind speed retrieval data and is limited to wind speeds up to 20 m/s. Therefore, a new GMF, denoted CSARMOD2, was developed to explore SAR-measured NRCS and wind vector data [18]. Scenes of RADARSAT-2 and Sentinel-1A SAR data are collocated with wind speed and wind direction measurements provided by NDBC buoys. Moreover, when Chinese Gaofen- (GF-) 3 SAR was launched, a good consistency of retrieved SAR wind speed and buoy in situ measurements is present using CMOD5.N, COMD7, and others. Several methodologies of wind retrieval are also developed using GF-3 copolarized and cross-polarized SAR data [19–21].

Although a series of wind speed retrieval algorithms are proposed in the past decades, the new algorithm is still a research highlight in retrieval processing. In particular, the empirical relationship between NRCS and wind speed was constantly revised using different operated SAR measurements. However, the sea state factor also influences the radar echo of the sea surface. It is known that the sea surface roughness caused by local winds contributes to the NRCS. Besides, the modulation of wind-generated small-scale roughness by swell waves can also modify the distribution of the sea surface slope, thereby, influencing the total NRCS of the sea surface. So, the influence of swell on NRCS would accordingly impact wind speed. In order to acquire a precise wind field, it is significant to further discuss and compensate for the influence of a swell wave in retrieval processing.

The paper is organized as follows. The collocated dataset, as well as the CMOD series functions, is briefly introduced in Section 2. In Section 3, the influence of pure swell on a two-dimensional sea surface slope and NRCS are demonstrated, together with a new strategy for wind speed retrieval. Then, the discussion and conclusion is given in Sections 4 and 5, respectively.

Table 1: Parameters of ENVISAT ASAR wave mode SLC imagery used in this paper.

Parameters	Values
Band	C (5.3 GHz)
Polarization	VV
Incidence angle θ	23°
Azimuth spacing	4.0 m
Range spacing	7.0 m
Swath width	5 km

2. Materials and Methods

2.1. ENVISAT ASAR Data. About 1647 scenes of ENVISAT ASAR Single Look Complex (SLC) imagery were collected from January of 2011, and were further matched with ECMWF data and buoy data. The parameters of used SLC data details are listed in Table 1. Among all of the operation modes of ENVISAT ASAR, the wave mode data were acquired with a fine resolution of 10 m and can provide continuous images of the sea surface within each 100 km. More than 2500 scenes of wave mode imagery are acquired everyday, which provides benefits for sea surface wind vector field retrieval. The used ENVISAT ASAR wave mode imagery is shown in Figure 1.

2.2. Buoy and ECMWF Reanalysis Data. The buoy and ECMWF reanalysis data are widely used as validation samples for sea surface remote sensing retrieval. The buoy measurements are provided by the National Data Buoy Center (NDBC), and the valid scope of a buoy is usually set as 30 min in time and 50 km in distance. The ERA-Interim reanalysis data are provided by European Centre for Medium-Range Weather Forecasts (ECMWF). It is noticed that the temporal and spatial resolutions are 6 h and $0.125^\circ \times 0.125^\circ$, respectively. Considering the occasional absence of buoy in situ measurements, the provided wind field (u10, v10) and other ocean dynamic parameters from the above two kinds of data sources can be used together as validation samples for sea surface remote sensing retrieval.

Figure 2 shows the wind vector comparison of buoy and ECMWF reanalysis data. The correlations between buoy and ECMWF data were 0.82 and 0.97 for both wind speed and wind direction, respectively. It can be seen that trustworthy results are present between buoy measurement and ECMWF reanalysis data. To use buoy and ECMWF reanalysis data is reliable for processing the in situ wind vector field [22].

2.3. CMOD Function. CMOD functions are originally derived from scatterometers, and the sea surface backscatter signals from space-borne measurements are related with incidence angle, wind speed, and wind direction [23]. A general type of CMOD function is presented as follows:

$$\sigma^0 = b_0(\theta, v)[1 + b_1(\theta, v)\cos\phi_w + b_2(\theta, v)\cos 2\phi_w]^n, \quad (1)$$

where σ^0 represents the space-borne measured NRCS of the

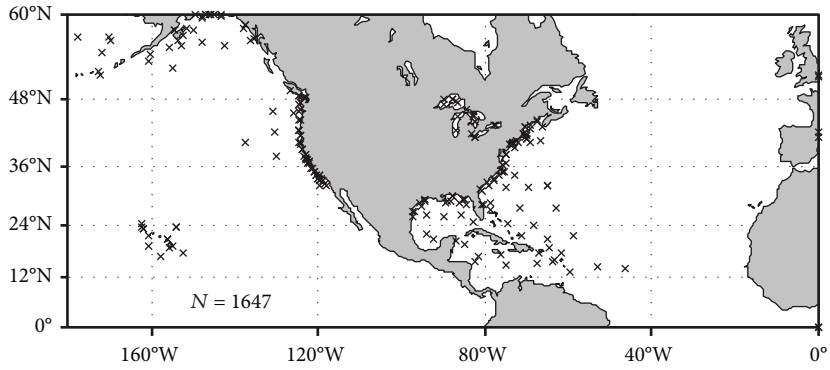

Figure 1: Map of collected ASAR WV imagery and buoy location.

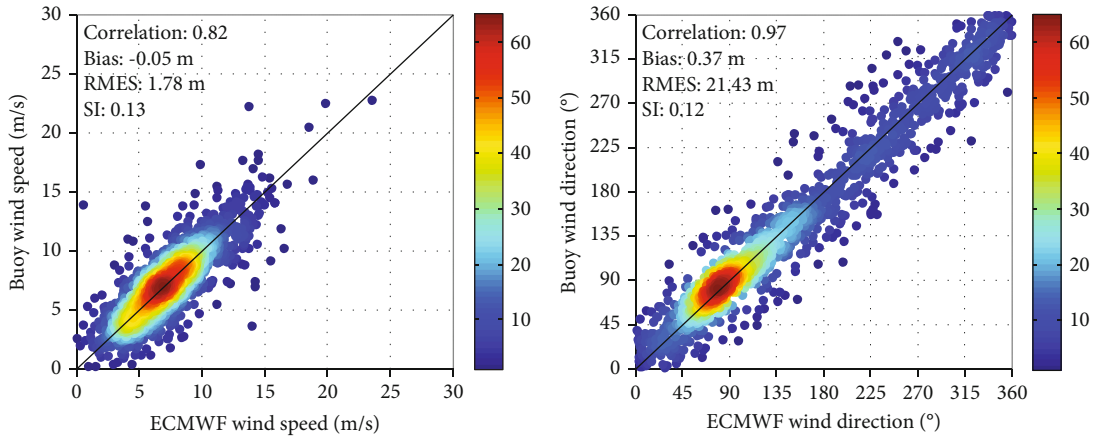

(a) Wind speed (b) Wind direction

Figure 2: Comparison of ECMWF wind vector with buoys.

sea surface, θ represents the incidence angle, v represents the wind speed, ϕ_w represents the relative wind direction between real wind direction and radar antenna pointing direction. b_0, b_1, and b_2 represent the functions of θ and v, which are recalculated by collocated ECMWF reanalysis wind data, NDBC buoy in situ wind measurements, and space-borne scatterometers (SAR). n represents the function power variable, which usually takes the value of 1.6. Actually, the wind speed and wind direction, as a couple of unknown terms, cannot be resolved on a basic set of incidence angle and NRCS. So, a general method of wind speed retrieval is to use external wind direction data as input, together with incidence angle, to acquire wind speed. Taking CMOD5.N, COMD-IFR2, and CSARMOD2, for example, the NRCS variation with an increase in wind speed and wind direction are shown in Figure 3.

In Figure 3(a), the incidence angle is set to 23°, and the relative wind direction is set to 0° (upwind direction). It can be seen that different CMOD functions behave in a similar curve characteristic, which increases as the wind speed increases. However, as the wind speed increases, the gap between the NRCS of CMOD5.N, COMD-IFR2, and CSARMOD2 becomes more and more remarkable, especially when the wind speed goes beyond 15 m/s. It has been verified that the COMD-IFR2 function behaves much better than others in the case of low and medium wind speeds (below 20 m/s). Besides, CMOD5.N presents a good performance in high wind speed cases (above 20 m/s), and CSARMOD2 seems to be comprised of something between CMOD-IFR2 and CMOD5.N in terms of NRCS. Figure 3(b) shows the azimuth distribution of the NRCS of CMOD5.N, COMD-IFR2, and CSARMOD2. The incidence angle is set to 23°, and the wind speed is set to 5 m/s. An approximate cosine shape is presented as an increase of relative wind direction. No matter if it is in an upwind, downwind, or cross-wind direction, the NRCS of CMOD5.N is still below that of COMD-IFR2 and CSARMOD2. And the NRCS of CMOD-IFR2 greatly exceeds that of CSARMOD2 in the up- and downwind directions, and it stays the same in the cross-wind direction. Although the CMOD5.N, COMD-IFR2, CSARMOD2, and other CMOD functions have been explored, it still remains arguable in wind speed retrieval using space-borne scatterometers or SAR data.

3. Results

3.1. NRCS Simulation under Different Sea States. For wind speed retrieval from C-band SAR imagery at VV polarization, the empirical relationship between NRCS and wind speed, wind direction, and incidence angle is established in

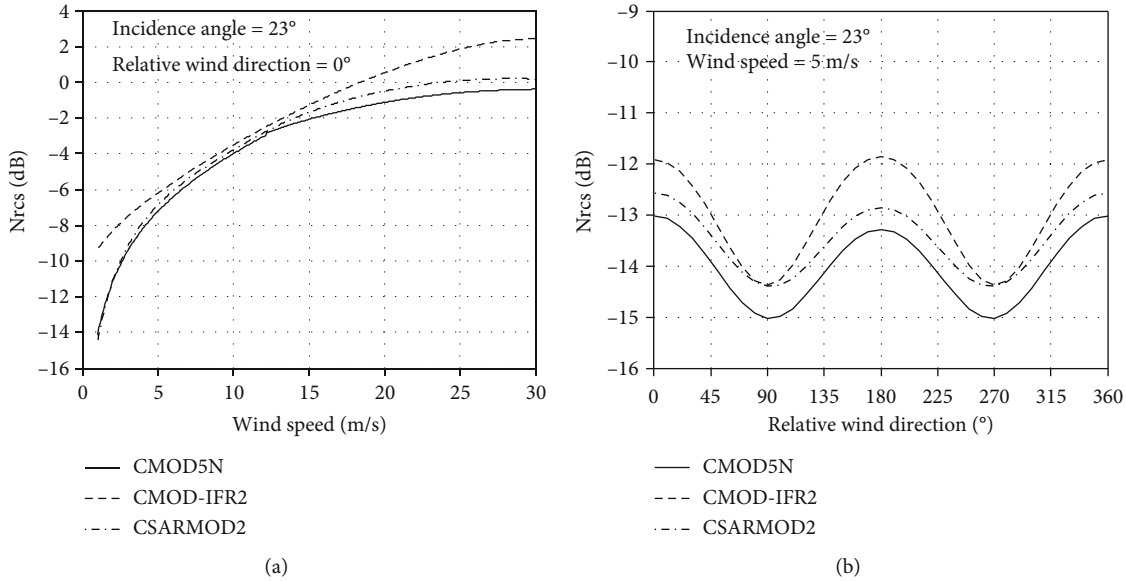

Figure 3: CMOD function backscattering characteristics: (a) CMOD function variation with wind speed; (b) CMOD function variation with wind direction.

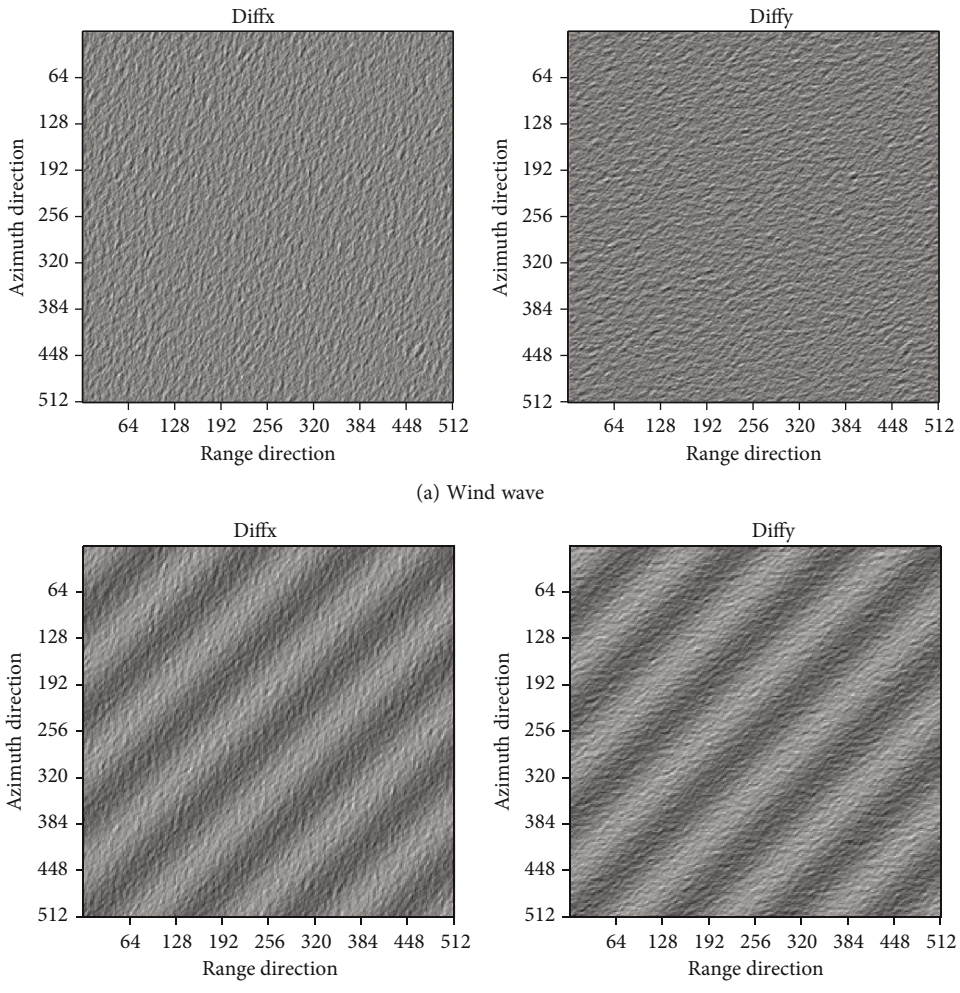

Figure 4: Two-dimensional sea surface slope: (a) wind speed = 5 m/s, wind direction = 45°; (b) wind speed = 5 m/s, wind direction = 45°, swell height = 2 m, swell direction = 45°, swell peak wavelength = 200 m.

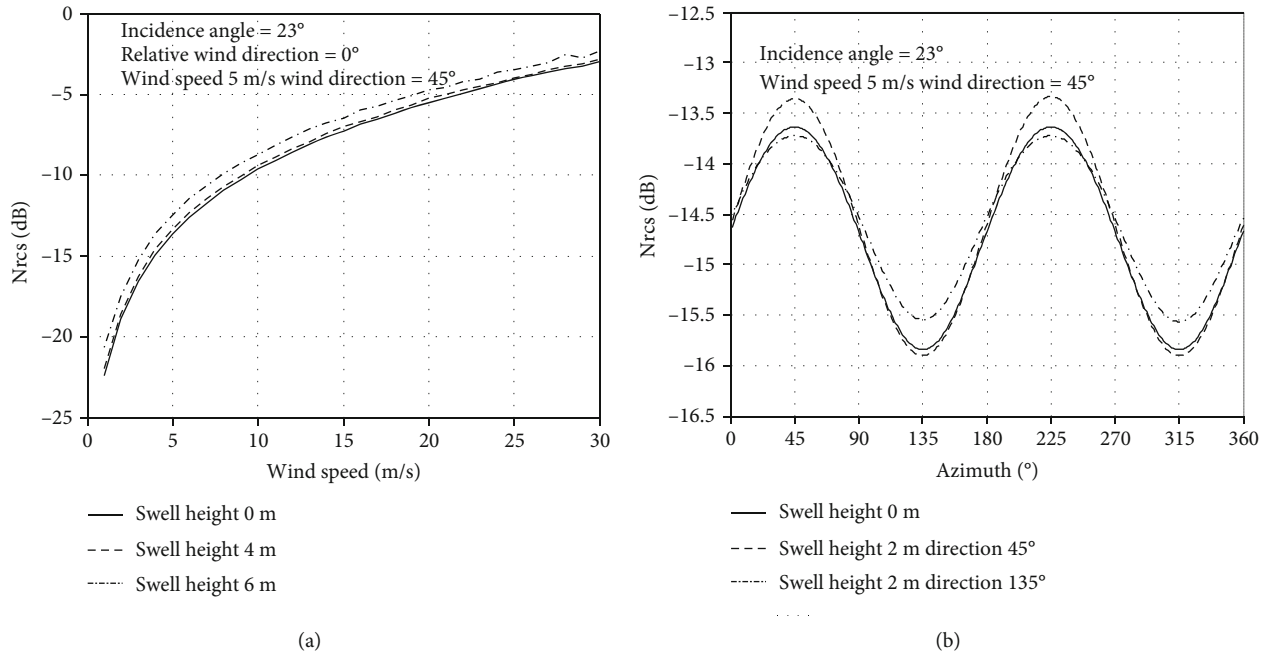

Figure 5: NRCS variation with wind speed and relative wind direction. (a) NRCS curves of upwind direction with swell heights of 0 m, 4 m, and 6 m, respectively. (b) NRCS curves of upwind direction with a swell height of 0 m, a swell height of 2 m, a swell direction of 45°, a swell height of 2 m, and a swell direction of 135°, respectively.

CMODs. However, the influence of sea state is usually neglected in processing SAR imagery due to sea surface large-scale statics. Actually, the sea state consists of wind wave caused by wind, and pure swell wave caused by external propagation. CMODs directly use the NRCS of the sea surface as the total sea surface backscatter signal to retrieve wind speed, without consideration of the influence of a pure swell wave on NRCS. That is why the retrieval accuracy of wind speed deteriorates in some sea zones. Here, the NRCS characteristics under different sea states are simulated to assess the influence of a pure swell. According to the composite Bragg scattering model, the total ocean surface NRCS consists of the Bragg scattering component of σ_{br}^{p} and the quasispecular scattering component of σ_{sp} [24]. It is noted that the influence of breaking waves are neglected, which has outstanding performance in high incidence angles [25].

$$\sigma_0^p = \sigma_{\mathrm{br}}^p + \sigma_{\mathrm{sp}}. \tag{2}$$

According to the Bragg resonance scattering mechanism, the Bragg scattering component σ_{br}^{p} is presented as follows: [26]:

$$\sigma_{\mathrm{br}}^p = 16\pi k^4 \left|G_p(\theta)\right|^2 F_r(k_{\mathrm{br}}, \varphi), \tag{3}$$

where k represents the radar wavenumber, G_p represents the Bragg scattering coefficients, θ represents the incidence angle, F_r represents the two-dimensional wave spectrum, k_{br} represents the Bragg wavenumber $k_{\mathrm{br}} = 2k \sin(\theta)$, φ represents the azimuth direction, p represents the polarization status.

The quasispecular scattering component σ_{sp} dominates in small incidence angles, which can be presented as follows [27]:

$$\sigma_{\mathrm{sp}} = |R_{\mathrm{eff}}|^2 \pi \sec^4\theta p(\zeta_x, \zeta_y), \tag{4}$$

where R_{eff} represents the effective reflection coefficient, p represents the slope probability density distribution function of specular points, $\zeta_x = \tan\theta \cos\varphi_w$ and $\zeta_y = -\tan\theta \sin\varphi_w$ are downwind and upwind slopes, respectively. The sea surface slope in range and azimuth direction are presented in Figure 4.

Figure 4(a) shows the two-dimensional sea surface slope in the case of a wind speed of 5 m/s and a wind direction of 45°, and Figure 4(b) shows the two-dimensional sea surface slope in the same wind field, together with a swell height of 2 m, a swell direction of 45°, and a swell peak wavelength of 200 m. It can be seen that the wind-induced sea surface slope in range and azimuth direction in Figure 4(a) is clearly distinguished from the wind and pure swell comodulated sea surface slope in Figure 4(b). The waves, especially the pure swell wave, modify the sea surface slope distribution which follows a Gaussian shape. It is noticed that wave breaking is neglected in this section, which induces the high-order no-Gaussian terms [28, 29]. Figure 5 shows the difference between simulated NRCS and sea state.

As shown in Figure 5(a), the NRCS increased as wind speed increased, showing a similar tendency with the CMODs in Figure 3. However, an approximate constant of NRCS appears with the influence of the swell wave, and a positive correlation relationship between an NRCS

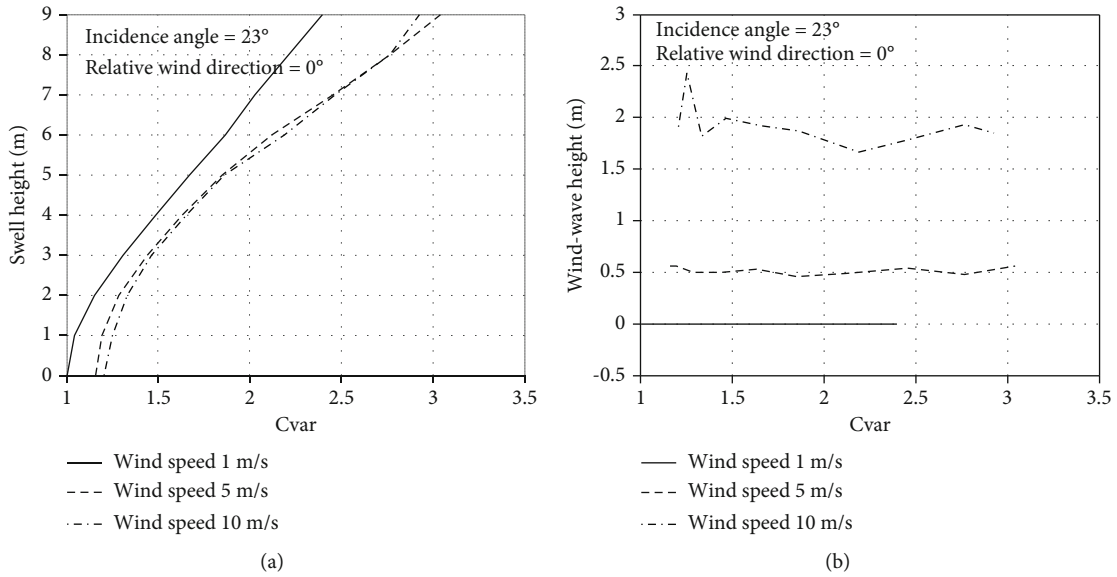

Figure 6: Sea surface height with an increase of Cvar. (a) Swell wave height variation with an increase of Cvar in the case of wind speeds of 1 m/s, 5 m/s, and 10 m/s. (b) Wind wave height variation with an increase of Cvar in the case of wind speeds of 1 m/s, 5 m/s, and 10 m/s. The simulated incidence angle is set to 23°, and relative wind direction is set to upwind.

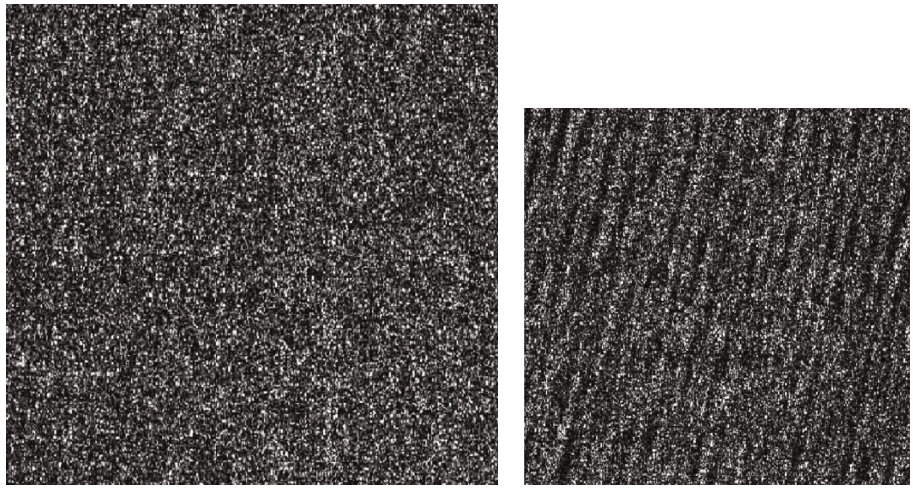

Figure 7: ENVISAT ASAR wave mode imagery in different sea states. (a) Pure wind wave: wind speed—7 m/s; Shsw—0 m. (b) Wind wave + swell wave: wind speed—7 m/s; Shsw—3 m.

increment and swell height is present. The influence of swell on azimuthal NRCS is shown in Figure 5(b). It is obvious that a positive effect is investigated on sea surface NRCS in an upwind direction, which is opposite a cross-wind direction. As a conclusion, the influence of the swell wave on the modulation of sea surface wind-induced NRCS is clearly in our simulation. With the aim to improve the retrieval accuracy of wind speed, it is significant to consider the swell modulation in wind-induced NRCS in CMODs [30].

3.2. Influence of Swell on Wind Speed Retrieval. Due to the absence of straight swell wave measurement in reality for wind speed retrieval, an imagery parameter of image variance (Cvar) is set to describe the influence of a swell wave [31]:

$$\text{Cvar} = \left(\text{std}\left(\frac{I - \langle I\rangle}{\langle I\rangle}\right)\right)^2, \quad (5)$$

where $\langle I\rangle$ present the average value of the SAR intensity imagery. In order to evaluate the sensitivity of Cvar on swell and wind wave height, the Elfouhaily spectrum is suggested to simulate the wind wave and swell wave spectrum and further explore the correlation between Cvar of corresponding simulated SAR imagery and sea state [32]. Figure 6 shows the variation of swell wave and wind wave height with an

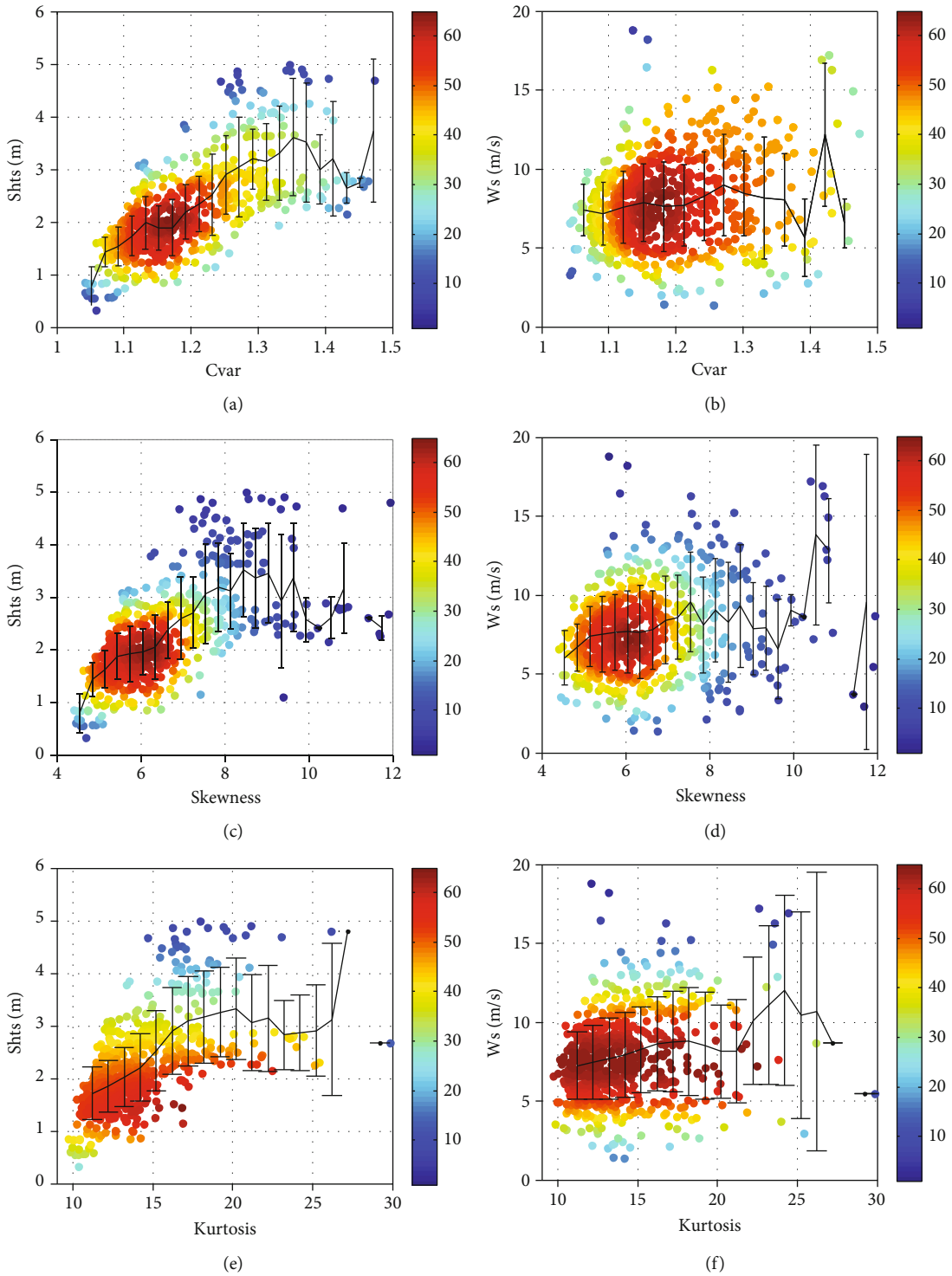

Figure 8: Relationship between sea state and SAR imagery parameters. Images in (a), (c), and (e) present the correlation between Shts and imagery parameters of Cvar, skewness and kurtosis. Images in (b), (d), and (f) present the correlation between wind speed and imagery parameters of Cvar, skewness, and kurtosis.

increase of Cvar. Both Figures 6(a) and 6(b) are simulated in an upwind direction and at an incidence angle of 23°. Clearly, a quasilinear curve between the simulated swell wave height and Cvar is found, which means that Cvar can be performed as an imagery characterization for swell information. On the contrary, the wind wave height cannot represent any remarkable variation as an increase of Cvar.

To further assess the influence of swell wave on NRCS, the ENVISAT ASAR wave mode imagery is calibrated and geometric. Collocated with ECMWF data, the wave streak

Table 2: Retrieval error metrics for the development of different empirical models varying the input parameters using ECMWF independent colocations not used in training of the empirical model.

Model	N	COR	BIAS (m/s)	RMSE (m/s)	SI
$F = (\sigma_0, \theta, \phi)$	3	0.84 (±0.03)	0.27 (±0.15)	1.55 (±0.34)	0.08 (±0.03)
$F = (\sigma_0, \theta, \phi$, Cvar)	4	0.86 (±0.01)	0.29 (±0.10)	1.43 (±0.11)	0.05 (±0.04)
$F = (\sigma_0, \theta, \phi$, Cvar, skewness)	5	0.86 (±0.01)	0.27 (±0.17)	1.47 (±0.13)	0.08 (±0.06)
$F = (\sigma_0, \theta, \phi$, Cvar, skewness, kurtosis)	6	0.85 (±0.01)	0.22 (±0.14)	1.46 (±0.06)	0.06 (±0.04)

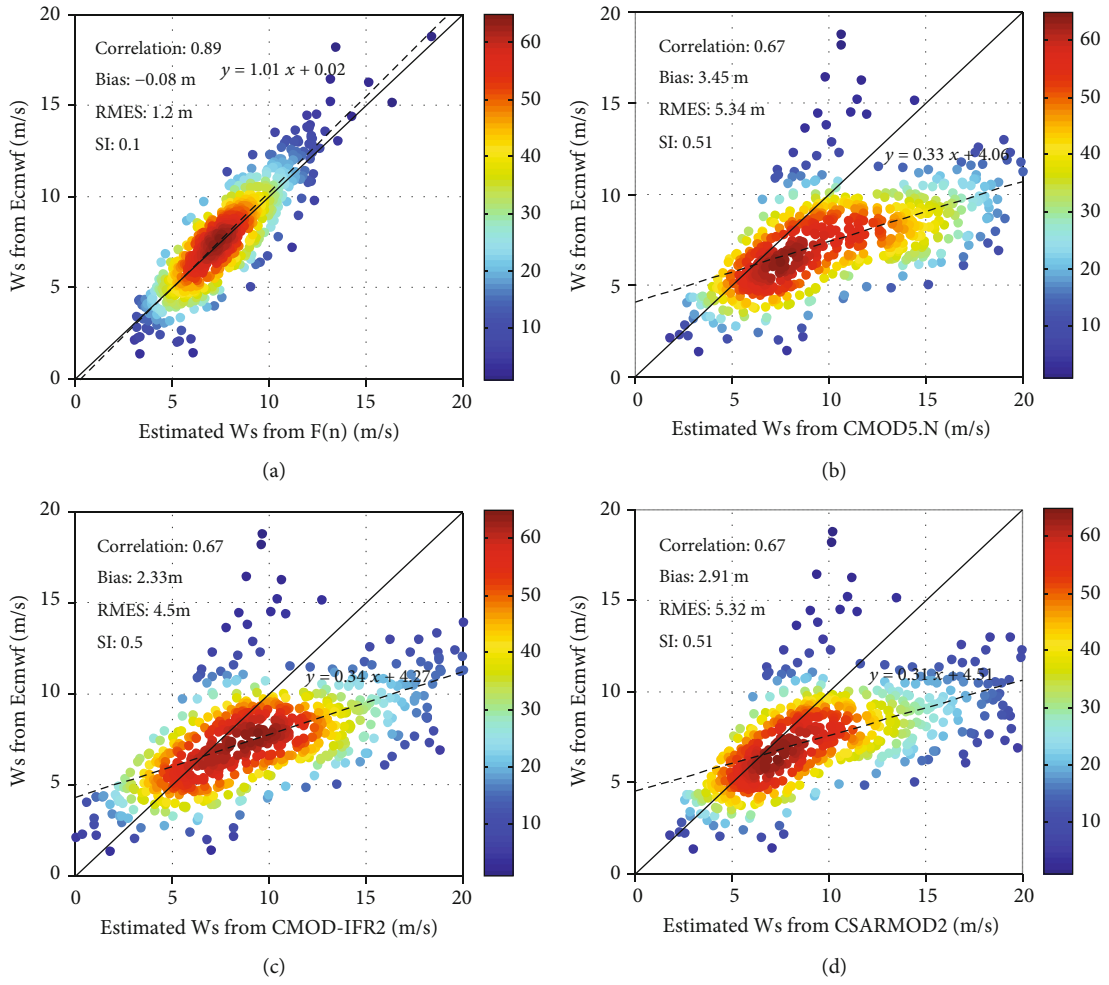

Figure 9: Wind speed comparison of ECMWF and developed empirical functions: (top row) F(N) and (bottom row) CMOD5.N for (left column) CMOD-IFR2 and (right column) CSARMOD2. Colors represent the density of scattering points: the solid red line represents a one-to-one line, and the dotted line represents a least square linear regression.

of SAR imagery under different sea states are shown in Figure 7. It can be seen that the swell wave is clearly distinguished from Figure 7(b), which is under a sea condition of 3 m of significant height of swell wave (Shsw) and a 7 m/s wind speed. In Figure 7(a), there is a pure wind wave with the same wind speed of 7 m/s, but the wave streak is not recognizable with the swell wave. It is concluded that the Cvar imagery can be used to assess the Shsw directly from SAR imagery.

With the aim of investigating the influence of swell state on wind speed retrieval without any external data, the swell geography parameters, especially the significant swell wave height, need to be parameterized from SAR imagery first. Besides Cvar, the higher-order features are also considered by skewness and kurtosis of the radar cross section [33]. The imagery parameters of Cvar, skewness, and kurtosis are together analyzed as a function of significant swell wave and wind speed, and the empirical relationship is fitted for a given incidence angle shown in Figure 8.

Figure 8 shows the relationship between sea state and SAR imagery parameters. Colors represent the density of scattering points, and the black line represents the error estimation. It appears that the performance of correlation

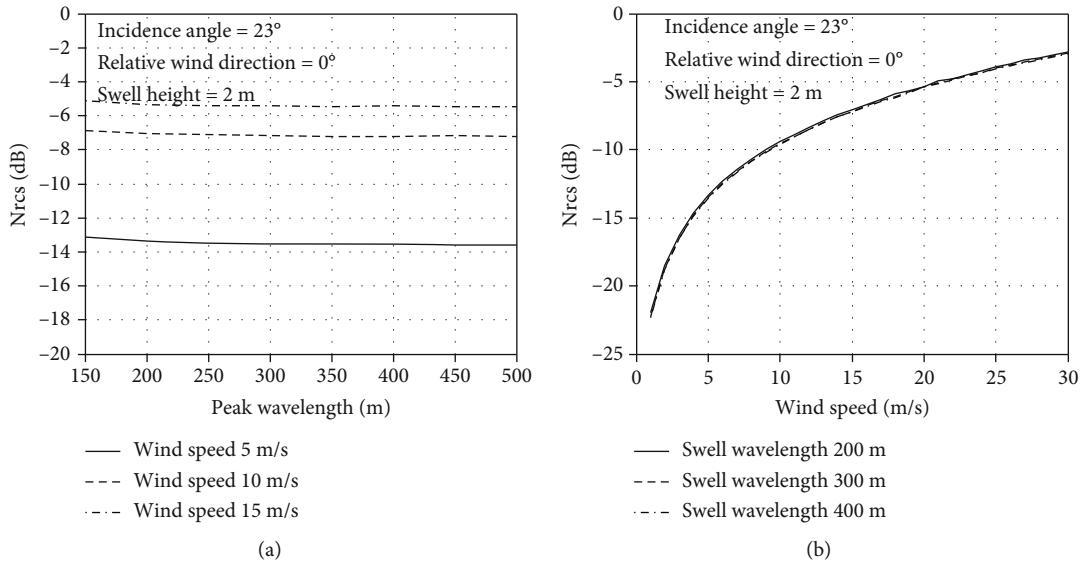

Figure 10: Influence of wave peak wavelength on NRCS.

between imagery parameters of Cvar, skewness, kurtosis, and Shts behaves much better than wind speed. Compared with skewness and kurtosis, Cvar is more responsive to the characteristics of a swell. In terms of wind speed retrieval, it is suggested to add parameters of Cvar, skewness, and kurtosis to compensate for the loss of the influence of a swell wave on NRCS.

3.3. New Method for Wind Speed Retrieval. A quasilinear relationship is observed in the relationship with Shts, as shown in Figures 7(a), 7(c), and 7(e). In consideration of the influence of a swell wave on wind speed retrieval, a new empirical model is proposed, taking a unique formulation as follows [34, 35]:

$$\mathrm{Ws} = A_0 + \sum_{i=1}^{n} A_i \times S_i + \sum_{i,j=1}^{n} A_{i,j} \times S_i \times S_j, \tag{6}$$

where S_i denote the SAR-derived parameters, A_i denote the tuning coefficients. Using the empirical relationship established by the training dataset, the rest of the verification dataset is used to assess the model precision. As shown in Table 2, the retrieval error metrics for the development of different empirical models varying the input parameters are compared. It appears that the model precision of F(n) improved as the model parameters increase. When Cvar is used as input, there is a significant improvement compared to the other functions that use three input parameters. Besides, as the parameters of skewness and kurtosis are used as input, the performance of function robustness behaves much better than others.

3.4. Validation with CMODs. The CMOD model is widely used for wind speed retrieval no matter if it is for a scatterometer or SAR. In this section, the F(n) model is compared with CMOD functions using collocated SAR and SWH dataset. Figure 9(a) shows the wind speed comparison between the F(n) model and collocated ECMWF data. Figures 9(b)–9(d) show the retrieval precision of CMOD5.N, CMOD-IFR2, and CSARMOD2 using the same dataset, respectively. Colors represent the density of scattering points. The black solid line represents the one-to-one line, and the dotted line represents the least square regression line. It appears that the least squares regression line agrees nicely with the one-to-one fit in Figure 9(a). The F(n) model performs much better than other CMOD functions, with a correlation of 0.89, a bias of 0.08, an RMSE of 1.2 m/s, and an SI of 0.1. An underestimation is present for models of CMOD5.N, CMOD-IFR2, and CSARMOD2 in conditions where wind speed is great than 5 m/s.

4. Discussion

Another important issue of the influence of swell peak wavelength on NRCS is also investigated in this session. Figure 10(a) shows the NRCS variation with an increase of wave peak wavelength in the case where wind speed is set to 5 m/s, 10 m/s, and 15 m/s, respectively. Barely no change of NRCS is shown in a fixed wind speed. A similar relationship is also shown in Figure 8(b). The NRCS grows with an increase of wind speed under different wave peak wavelengths. It can be noticed that a minimum bias of NRCS can be found between different swells of peak wavelengths.

It has been noticed that the azimuth cutoff wavelength was also regarded as the imagery features caused by moving the sea surface. To explore the impact of azimuth cutoff wavelength on NRCS, the correlation between azimuth cutoff wavelength and NRCS is shown in Figure 11. As shown in Figure 11, there is a high correlation between azimuth cutoff wavelength and SWH.

Unfortunately, an azimuth cutoff wavelength still cannot distinguish SWH from a swell wave and a wind wave. For now, few studies are focused on the impact of azimuth cutoff wavelength on swell-wind wave interaction. So, in a future

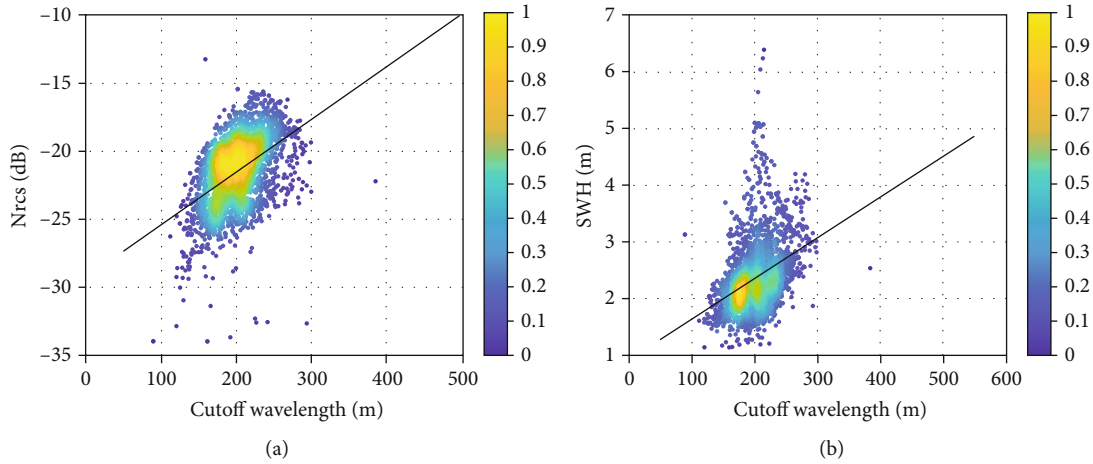

Figure 11: Image in (a) represents the relationship between azimuth cutoff wavelength and NRCS. Image in (b) represents the relationship between azimuth cutoff wavelength and SWH.

study, we are mainly interested in using an imagery parameter to represent the impact of swell wave to ocean surface scattering.

5. Conclusions

In this paper, the influence of swell on wind speed retrieval is investigated. The NRCS scene under different sea states is simulated to explore the relationship between NRCS variation with swell height, together with swell direction. It is concluded that a positive effect is investigated on sea surface NRCS in an upwind direction, which is opposite in a cross-wind direction. To explore the influence of swell on wind speed retrieval, a new empirical algorithm is proposed to retrieve wind speed from SAR imagery, namely, the F(n) model. Besides the CMOD parameters of NRCS, incidence angle, and relative wind direction, the imagery parameters of Cvar, skewness, and kurtosis are used to compensate for the influence of swell on wind speed retrieval using SAR imagery. Moreover, the collocated ECMWF wind speed dataset and ENVISAT ASAR wave mode imagery are used to verify the new model for wind speed retrieval.

It is concluded that the F(n) model used in this paper performs much better than CMOD functions, such as CMOD5.N, CMOD-IFR2, and CSARMOD2.

It is also concluded that the F(n) model performs much better than other CMOD functions because of a correlation of 0.89, a bias of 0.08, an RMSE of 1.2 m/s, and an SI of 0.1. The empirical algorithm herein is applicable for retrieving wind speed from ENVISAT ASAR wave mode imagery. In the near future, more implementation and adaption are required for RADARSAT-2, Sentinel-1, and Chinese GF-3 SAR.

Data Availability

The ASAR and ECMWF data used to support the findings of this study are included within the article. The authors would like to thank ESA for providing the ASAR data (http://datashare.rsgs.ac.cn/). The authors would like to thank the European Centre for Medium-Range Weather Forecasts (ECMWF) for providing the reanalysis data (http://www.ecmwf.int/en/research/climate-reanalysis/browse-reanalysis-datasets).

Conflicts of Interest

The authors declare no conflict of interest.

Acknowledgments

This research was funded by the National Natural Science Foundation of China (grant number 61731022). ECMWF wave fields were accessed via http://www.ECMWF.int.

References

[1] Q. Yan, J. Zhang, J. M. Meng, J. Wang, and C. Fan, "Use of an optimum interpolation method to construct a high-resolution global ocean surface vector wind dataset from active scatterometers and passive radiometers," *International Journal of Remote Sensing*, vol. 38, no. 20, pp. 5569–5591, 2017.

[2] A. Nekrasov and P. Hoogeboom, "A Ka-band backscatter model function and an algorithm for measurement of the wind vector over the sea surface," *IEEE Geoscience and Remote Sensing Letters*, vol. 2, no. 1, pp. 23–27, 2005.

[3] Y. Ren, S. Lehner, S. Brusch, X. Li, and M. He, "An algorithm for the retrieval of sea surface wind fields using X-band TerraSAR-X data," *International Journal of Remote Sensing*, vol. 33, no. 23, pp. 7310–7336, 2012.

[4] X. M. Li and S. Lehner, "Algorithm for sea surface wind retrieval from TerraSAR-X and TanDEM-X data," *IEEE Transactions on Geoscience and Remote Sensing*, vol. 52, no. 5, pp. 2928–2939, 2014.

[5] L. Ren, J. Yang, A. Mouche et al., "Preliminary analysis of Chinese GF-3 SAR quad-polarization measurements to extract winds in each polarization," *Remote Sensing*, vol. 9, no. 12, p. 1215, 2017.

[6] S. Weizeng, S. Yexin, and S. Jian, "Preliminary assessment of wind and wave retrieval from Chinese Gaofen-3 SAR imagery," *Sensors*, vol. 17, no. 8, p. 1705, 2017.

[7] B. Zhang, S. Fan, A. Mouche, G. Zhang, and W. Perrie, "Synergistic measurements of hurricane wind speeds and directions from C-band dual-polarization synthetic aperture radar," in *2019 IEEE International Geoscience and Remote Sensing Symposium*, Yokohama, Japan, 2019.

[8] G. Zhang, X. Li, W. Perrie, P. A. Hwang, B. Zhang, and X. Yang, "A hurricane wind speed retrieval model for C-band RADARSAT-2 cross-polarization ScanSAR images," *IEEE Transactions on Geoscience & Remote Sensing*, vol. 55, no. 8, pp. 4766–4774, 2017.

[9] A. E. Long, "Towards a C-band radar sea echo model for the ERS-1 scatterometer," in *First ISPRS Colloquium on Spectral Signatures in Remote Sensing*, pp. 29–34, International Society for Photogrammetry and Remote Sensing, Les Arcs, 1985.

[10] A. Stoffelen and D. Anderson, "Scatterometer data interpretation: estimation and validation of the transfer function CMOD4," *Journal of Geophysical Research: Oceans*, vol. 102, no. C3, pp. 5767–5780, 1997.

[11] A. Bentamy, P. Queffeulou, Y. Quilfen, and K. Katsaros, "Ocean surface wind fields estimated from satellite active and passive microwave instruments," *IEEE Transactions on Geoscience and Remote Sensing*, vol. 37, no. 5, pp. 2469–2486, 1999.

[12] H. Hersbach, A. Stoffelen, and S. D. Haan, "An improved C-band scatterometer ocean geophysical model function: CMOD5," *Journal of Geophysical Research: Oceans*, vol. 112, no. C3, pp. 225–237, 2007.

[13] A. Verhoef, M. Portabella, A. Stoffelen, and H. Hersbach, *CMOD5.n—The CMOD5 GMF for Neutral Winds*, KNMI, De Bilt, The Netherlands, 2008, Ocean Sea Ice SAF Tech. Note SAF/OSI/CDOP/KNMI/TEC/TN/3.

[14] L. Ricciardulli, T. Meissner, and F. Wentz, "Towards a climate data record of satellite ocean vector winds," in *Geoscience and Remote Sensing Symposium (IGARSS), 2012 IEEE International*, pp. 2067–2069, New York, 2012.

[15] S. Soisuvarn, Z. Jelenak, P. S. Chang, S. O. Alsweiss, and Q. Zhu, "CMOD5.H—a high wind geophysical model function for C-band vertically polarized satellite scatterometer measurements," *IEEE Transactions on Geoscience and Remote Sensing*, vol. 51, no. 6, pp. 3744–3760, 2013.

[16] A. Elyouncha, X. Neyt, A. Stoffelen, and J. Verspeek, "Assessment of the corrected CMOD6 GMF using scatterometer data," in *Remote Sensing of the Ocean, Sea Ice, Coastal Waters, and Large Water Regions*, no. article 963803, 2015SPIE, Toulouse, 2015.

[17] A. Stoffelen, J. A. Verspeek, J. Vogelzang, and A. Verhoef, "The CMOD7 geophysical model function for ASCAT and ERS wind retrievals," *IEEE Journal of Selected Topics in Applied Earth Observations and Remote Sensing*, vol. 10, no. 5, pp. 2123–2134, 2017.

[18] A. Mouche and B. Chapron, "Global C-Band Envisat, RADARSAT-2, and Sentinel-1 SAR measurements in copolarization and cross-polarization," *Journal of Geophysical Research Oceans*, vol. 120, no. 11, pp. 7195–7207, 2015.

[19] H. Wang, J. Yang, A. Mouche et al., "GF-3 SAR ocean wind retrieval: the first view and preliminary assessment," *Remote Sensing*, vol. 9, no. 7, p. 694, 2017.

[20] L. Wang, B. Han, X. Yuan et al., "A preliminary analysis of wind retrieval, based on GF-3 wave mode data," *Sensors*, vol. 18, no. 5, p. 1604, 2018.

[21] W. Shao, S. Zhu, X. Zhang et al., "Intelligent wind retrieval from Chinese Gaofen-3 SAR imagery in quad polarization," *Journal of Atmospheric and Oceanic Technology*, vol. 36, no. 11, pp. 2121–2138, 2019.

[22] L. Ren, J. Yang, A. A. Mouche et al., "Assessments of ocean wind retrieval schemes used for Chinese Gaofen-3 synthetic aperture radar co-polarized data," *IEEE Transactions on GeoScence and Remote Sensing*, vol. 57, no. 9, pp. 7075–7085, 2019.

[23] W. Yong, "Exploitable wave energy assessment based on ERA-interim reanalysis data—a case study in the East China Sea and the South China Sea," *Acta Oceanologica Sinica*, vol. 34, no. 9, pp. 143–155, 2015.

[24] W. Shao, X. Li, and X. Yang, "Retrieval of winds and waves from synthetic aperture radar imagery," in *Remote Sensing of the Asian Seas*, V. Barale and M. Gade, Eds., pp. 285–303, Springer, Cham, 2019.

[25] P. A. Hwang, B. Zhang, J. V. Toporkov, and W. Perrie, "Comparison of composite Bragg theory and quad-polarization radar backscatter from RADARSAT-2: with applications to wave breaking and high wind retrieval," *Journal of Geophysical Research: Atmospheres*, vol. 115, no. C8, pp. 246–255, 2010.

[26] V. Kudryavtsev, D. Hauser, G. Caudal, and B. Chapron, "A semiempirical model of the normalized radar cross-section of the sea surface 1. Background model," *Journal of Geophysical Research: Oceans*, vol. 108, no. C3, pp. FET 2-1–FET 2-24, 2003.

[27] G. R. Valenzuela, "Theories for the interaction of electromagnetic and oceanic waves–a review," *Boundary-Layer Meteorology*, vol. 13, no. 1-4, pp. 61–85, 1978.

[28] D. E. Barrick, "Rough surface scattering based on the specular point theory," *IEEE Transactions on Antennas and Propagation*, vol. 16, no. 4, pp. 449–454, 1968.

[29] L. Wetzel, "On microwave scattering by breaking waves," in *Wave Dynamics and Radio Probing of the Ocean Surface*, pp. 273–284, Springer US, New York, 1986.

[30] P. H. Y. Lee, J. D. Barter, K. L. Beach et al., "Scattering from breaking gravity waves without wind," *IEEE Transactions on Antennas and Propagation*, vol. 46, no. 1, pp. 14–26, 1998.

[31] H. Li, A. Mouche, and J. E. Stopa, "Impact of sea state on wind retrieval from Sentinel-1 wave mode data," *IEEE Journal of Selected Topics in Applied Earth Observations and Remote Sensing*, vol. 12, no. 2, pp. 559–566, 2019.

[32] D. Gao, Y. Liu, J. Meng, Y. Jia, and C. Fan, "Estimating significant wave height from SAR imagery based on an SVM regression model," *Acta Oceanologica Sinica*, vol. 37, no. 3, pp. 103–110, 2018.

[33] T. Elfouhaily, B. Chapron, K. Katsaros, and D. Vandemark, "A unified directional spectrum for long and short wind-driven waves," *Journal of Geophysical Research: Oceans*, vol. 102, no. C7, pp. 15781–15796, 1997.

[34] V. Kerbaol, B. Chapron, and P. W. Vachon, "Analysis of ERS-1/2 synthetic aperture radar wave mode imagettes," *Journal of Geophysical Research*, vol. 103, no. C4, pp. 7833–7846, 1998.

[35] C. Fan, X. Wang, X. Zhang, and D. Gao, "A newly developed ocean significant wave height retrieval method from Envisat ASAR wave mode imagery," *Acta Oceanologica Sinica*, vol. 38, no. 9, pp. 120–127, 2019.